

An efficient method for calculating finite-difference seismograms after model alterations

Johan O. A. Robertsson* and Chris H. Chapman*

ABSTRACT

Seismic modeling, processing, and inversion often require the calculation of the seismic response resulting from a suite of closely related seismic models. Even though changes to the model may be restricted to a small subvolume, we need to perform simulations for the full model.

We present a new finite-difference method that circumvents the need to resimulate the complete model for local changes. By requiring only calculations in the subvolume and its neighborhood, our method makes possible significant reductions in computational cost and memory requirements. In general, each source/receiver location requires one full simulation on the complete model. Following these pre-computations, recalculation of the altered wavefield can be limited to the region around the subvolume and its neighborhood.

We apply our method to a 2-D time-lapse seismic problem, thereby achieving a factor of 15 reduction in computational cost. Potential savings for 3-D are far greater.

INTRODUCTION

Finite-difference (FD) methods provide an accurate means of computing seismograms for complex geologic models. Unfortunately, FD simulations can be computationally very expensive, thereby limiting their general use. Different approaches have been taken to make highly accurate numerical modeling methods such as FD schemes more efficient.

By combining methods appropriate for different wave-propagation regimes, e.g., ray theory or 1-D layered response, with an FD method, it is possible to increase considerably the computational efficiency as well as the simulation accuracy (Wu and Aki, 1988). Several such hybrid techniques have been developed for seismic applications (e.g., Drake, 1972; Kurkjian et al., 1994; Robertsson et al., 1996; Zahradník

and Moczo, 1996; Piserchia et al., 1998; and references therein).

A second approach to gain computational efficiency comprises grid-refinement or multigrid techniques. FD calculations are limited by either the shortest wavelengths that occur in the simulation model or the complexity of the model. The maximum grid-step size to achieve a sufficiently accurate solution is determined by the minimum of these two constraints. By using a finer grid in the parts of the model where the lowest seismic velocities or the highest structural complexity occur, a computationally efficient solution may be obtained (e.g., McLaughlin and Day, 1994; Robertsson and Holliger, 1997). Such grid refinement is of course implicit in higher overhead finite element methods.

Marfurt and Shin (1989) and Pratt (1999) describe how so-called nested dissection can be used for efficient solution of multiple-source problems in the frequency domain. If LU decomposition is used, the matrix factors can be reused to solve the forward problem rapidly for any new source vector in the wave equation. These techniques thus enable efficient solution of problems with multiple locations or, by using virtual sources, problems with a suite of closely related models. However, the matrix methods in the frequency domain are usually less efficient than explicit time-domain methods unless these features can be exploited.

In this paper, we present a fundamentally different time-domain FD methodology for efficiently computing the seismic response from a seismic model subject to one or several changes within subvolumes. The methodology is not based on perturbation theory in its traditional sense, in which scattering is considered from point perturbations and approximated by a Born series (Chapman and Coates, 1994). The methodology, in fact, is related more closely to the hybrid methods or multigrid techniques described above. However, if the scatterer comprises a much larger volume (a subgrid encompassing the subvolumes of change), then our method could be characterized in terms of a Born perturbation series (Schuster, 1985). In terms of scattering from the larger volumes, third-order terms are neglected. However, *within* the larger volumes, scattering

Published on Geophysics Online November 30, 1999. Manuscript received by the Editor May 22, 1998; revised manuscript received July 15, 1999.
*Schlumberger Cambridge Research Ltd., High Cross, Madingley Road, Cambridge CB3 0EL, United Kingdom. E-mail: jrobertsson@slb.com.; chapman@scr.slb.com.

© 2000 Society of Exploration Geophysicists. All rights reserved.

of all orders is included and no perturbation series approximation is needed. From now on, when referring to perturbation theory, we mean perturbations of point scatterers.

Initially, the response from a full reference model is calculated and the wavefield is recorded at receivers and along a closed surface around a subvolume (or multiple surfaces and subvolumes if there are several regions of change). As changes to the model occur inside the subvolume, the recorded seismograms can be updated by simulating the response on a small FD submesh encompassing the neighborhood of the subvolume. The method thus allows full FD simulations for the complete model to be corrected for local changes while requiring only calculations in the subvolume and its neighborhood, which significantly reduces the computational cost, in terms of the

number of calculations and the memory for storage of material parameters and variable fields. Again, the method is not based on perturbation theory (as discussed above); the changes in the model, therefore, can be arbitrarily large, and all orders of scattering are accounted for in the FD submesh. The entire interaction of the wavefield between the FD submesh and the full model before model alteration also is accounted for completely. The only part of the wavefield missing is that resulting from interactions of the *altered wavefield* with the unaltered model outside the submesh which propagate back into and are recorded in the submesh—what might be called second- (or higher) order, long-range interactions. The description would be more complicated if there are multiple submeshes.

We refer to the new method as the *FD-injection method*. After outlining the standard FD scheme, we describe the FD-injection method and its implementation. Next we illustrate the method on a time-lapse seismics example. Finally, we discuss various potential applications of the FD-injection method.

Table of symbols

x_i	Cartesian coordinates (x_1 horizontal and x_2 vertical)
σ_{ij}	Stress tensor
v_i	Particle velocity
$s_{ij}^{(m)}$	Memory variables for relaxation mechanism m
c_{ijkl}	Elastic stiffness tensor
ρ	Density
M	Number of viscoelastic relaxation mechanisms
$\tau_\varepsilon^{(m)}$	Strain relaxation time for relaxation mechanism m
$\tau_\sigma^{(m)}$	Stress relaxation time for relaxation mechanism m
G_{ik}	Velocity Green's tensor in unaltered model
Σ_{ijk}	Stress Green's tensor in unaltered model
f_k	Volume force
n_j	Normal to a surface
S_i	Surface that encloses altered region of model (injection surface)
V_i	Altered region of model (injection subvolume)
V_e	Full FD model outside V_i (volume exterior to V_i)
S	Surface that encloses FD submesh
V'	Part of V_e inside S
V''	Part of V_e outside S
S_e	Integration surface for propagating wavefield to distant receivers
S'_e	Part of S_e inside S
S''_e	Part of S_e outside S
σ_{ij}^u	Stress wavefield in unaltered model
v_i^u	Particle velocity wavefield in unaltered model
σ_{ij}^R	Recalculated stress wavefield on FD submesh
v_i^R	Recalculated particle velocity wavefield on FD submesh
\mathbf{m}	Model parameters throughout the model before alteration
\mathbf{m}^c	Model parameters throughout the model after alteration
C_{CPU}	Total computational cost for a suite of simulations
D	Required amount of disk space
K	Number of models subject to changes within V_i
R	Number of receivers outside FD submesh S
N	Spatial dimension in full FD mesh ($V_e \cup V_i$)
n	Spatial dimension in FD submesh ($V'_e \cup V_i$)
T	Number of time steps in simulation on full FD mesh
t	Number of time steps in simulation on FD submesh
a, b, c, d	Proportionality constants

FINITE-DIFFERENCE METHOD

We implement the FD-injection method by using a staggered FD scheme to solve the first-order partial differential equations for stress σ_{ij} and particle velocity v_i describing anisotropic, viscoelastic wave propagation in a 2-D Cartesian grid (horizontal coordinate x_1 and vertical coordinate x_2). The viscoelastic time convolutions are eliminated and replaced by multiplications by introducing so-called memory variables (e.g., Robertsson et al., 1994). The constitutive equations to update the stresses using M relaxation mechanisms for each relaxation function are:

$$\frac{\partial \sigma_{ij}}{\partial t} = \left(\frac{\tau_\varepsilon^{(m)}}{\tau_\sigma^{(m)}} - M + 1 \right) c_{ijkl} \frac{\partial v_k}{\partial x_l} + s_{ij}^{(m)}, \quad (1)$$

where c_{ijkl} are the elastic stiffnesses and $s_{ij}^{(m)}$ are the memory variables (M memory variables for each stress component) that determine the anelastic behavior of the material. Each relaxation mechanism is characterized by a stress and a strain relaxation time $\tau_\varepsilon^{(m)}$ and $\tau_\sigma^{(m)}$. These can be tuned to a desired level of attenuation (Blanch et al., 1995; Robertsson and Coates, 1997). The memory variables are governed by:

$$\frac{\partial s_{ij}^{(m)}}{\partial t} = -\frac{1}{\tau_\sigma^{(m)}} \left(s_{ij}^{(m)} + \left(\frac{\tau_\varepsilon^{(m)}}{\tau_\sigma^{(m)}} - 1 \right) c_{ijkl} \frac{\partial v_k}{\partial x_l} \right). \quad (2)$$

Finally, the equation of motion completes the system of equations that describe anisotropic, viscoelastic wave propagation:

$$\frac{\partial v_i}{\partial t} = \frac{1}{\rho} \frac{\partial \sigma_{ij}}{\partial x_j}, \quad (3)$$

where ρ is the density.

The stresses (and corresponding memory variables) and the particle velocities comprise the wavefield and are discretized functions of both time and space. Because of the staggering, they are not defined in exactly the same locations, but are shifted with respect to each other both in time and space, as

is illustrated in Figure 1. For simplicity, because we are using Cartesian grids and surfaces throughout the paper, we refer to the stress components as they appear in tractions on Cartesian surfaces, i.e., we call σ_{11} and σ_{22} the normal stresses and σ_{12} the shear stress. The normal stresses, σ_{11} and σ_{22} , have the same location in each grid cell. The shear stress component, σ_{12} , is staggered by half a grid step in both the x_1 - and x_2 -directions with respect to the normal stresses. The v_2 component is staggered half a grid step in the x_2 -direction from the normal stresses, whereas the v_1 component is staggered half a grid step in the x_1 -direction. All stresses are defined at the same levels in time, whereas the particle velocities are staggered with half a time step with respect to the stresses. A leapfrog scheme is used to update the stresses and particle velocities in time and a Crank-Nicholson scheme for the memory variables. A fourth-order accurate, centered scheme is used for approximating the spatial derivatives. A more complete description of this family of FD schemes has been presented by, for instance, Robertsson et al. (1994).

FINITE-DIFFERENCE INJECTION METHOD

We start with basic definitions of the terminology used to describe the FD-injection method. Regions where models are altered and in whose neighborhood FD solutions are recalculated are referred to as *injection subvolumes*. The terminology *injecting a wavefield* refers to introducing a wavefield recorded in a previous FD simulation along the closed *injection surface* defining the injection subvolume (this becomes the “source field” that drives the FD simulation). It is important to realize that the method is not based on perturbation theory as discussed in the introduction. Rather than satisfying certain boundary conditions, the principle of superposition and enforcing continuity of the superimposed wavefields form the basis of the injection.

The FD-injection method depends on connecting solutions in different regions. Several surfaces are therefore important in the FD-injection method (Figure 2). The surface S_i encloses the altered region of the model, the injection subvolume V_i . Exterior to this surface is the volume V_e (we will limit our

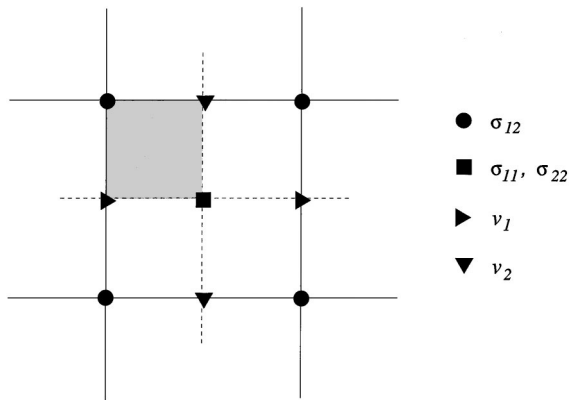


FIG. 1. The staggered FD-grid. Solid lines (one grid step apart) represent the grid during the update of σ_{12} . Dashed lines (one grid step apart) represent the grid during the update of σ_{11} and σ_{22} . During the update of particle velocities (half a time step later), the grids run through the v_1 and v_2 components. All wavefield quantities adjacent to the shaded area belong to the same grid cell.

discussion to simply connected regions for simplicity). Located inside the volume V_e and embedding V_i is the surface S which bounds the FD submesh used to calculate the altered solution. We denote the part of V_e inside S as V'_e and outside as V''_e , i.e.,

$$V_e = V'_e \cup V''_e. \quad (4)$$

Thus the FD submesh is $V'_e \cup V_i$, so that V_i is embedded inside the FD submesh. The surface S therefore limits the size of the FD submesh used in the calculations. Its only purpose is to act as an absorbing boundary condition (just as the boundary of the full FD mesh acts as an absorbing boundary). It must be larger than S_i so that the boundary conditions do not interfere with the FD solution within the injection subvolume V_i .

If the receivers are located outside the boundary S , i.e., outside the FD submesh, then between the injection subvolume V_i and the receivers we construct the surface S_e intersecting the FD submesh. The elastodynamic representation integral (Tan, 1975; Aki and Richards, 1980) allows the recalculated solution to be propagated from this surface to the receivers. In practice, the surface integral is restricted to the portion of this surface within the FD submesh, S'_e , resulting in possible truncation errors. For completeness, we refer to the part of S_e outside the FD submesh as S''_e , i.e.,

$$S_e = S'_e \cup S''_e. \quad (5)$$

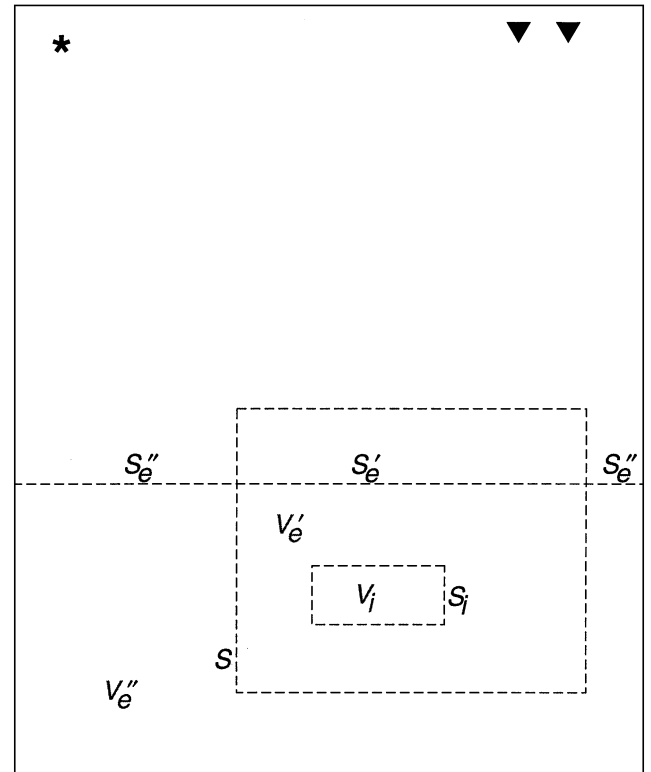


FIG. 2. The injection subvolume V_i is enclosed by the surface S_i . The model in the exterior volume V_e remains unchanged. The absorbing boundary of the FD submesh, S , lies in the unaltered volume V_e . If the receivers (triangles) are outside the FD submesh, then a surface S_e is defined between the model alterations and the receivers. The surface integral is restricted to the portion S'_e within the submesh. The source (star) generates the injection wavefield.

Wavefield injection

The most critical step in the FD-injection method is the technique for introducing a wavefield inside the FD grid. Alterman and Karal (1968), Kelly et al. (1976), and Levander (1989) have described how to introduce a source field into a FD grid by injecting an analytical source solution on a surface surrounding the point source to avoid the source singularity in the FD computation. Exactly the same technique can be used here on the surface S_i where now the surface encloses the region of model alterations (not the source). In both cases, the injection depends only on the wavefield continuity—in the referenced earlier work between an analytic source and an FD calculation, and in our case, between an FD “source field” and a new FD calculation. The other difference is that in the referenced work, the injection is from inside to outside the surface, whereas in our case, the geometry is reversed.

In principle, all we need is to satisfy the principle of superposition and the continuity of the superimposed wavefields across the injection surface, S_i . In practice, because the FD calculation in the submesh is discontinuous at the injection surface, some care must be taken in the FD calculations where the spatial FD stencil intersects the injection surface.

In the unaltered model, the solution is $\{v_i^I, \sigma_{ij}^I\}$. In the altered model, inside the FD submesh we define the recalculated solution to be $\{v_i^R, \sigma_{ij}^R\}$. As the recalculation is driven by injection of $\{v_i^I, \sigma_{ij}^I\}$ on S_i , it is discontinuous there (see Figures 10 and 11, below). The solution for velocity components is given by

$$v_i = v_i^R \quad \text{in } V_i, \quad (6)$$

$$= v_i^R + v_i^I \quad \text{in } V_e', \quad (7)$$

$$= v_i^I + \int_{S_e'} (G_{ik} * \sigma_{kj}^R - \Sigma_{ijk} * v_k^R) n_j dS \quad \text{in } V_e'', \quad (8)$$

where in equation (8), the quantities G_{ik} and Σ_{ijk} in the representation integral (Tan, 1975; Aki and Richards, 1980) are the velocity and stress Green's tensors from the observation point in V_e'' (solid triangles in Figure 2) to the point of integration, calculated in the unaltered model. The star denotes convolution in time, and n_j is the normal to the surface S_e' . The solution for the stress components can be expressed similarly.

During the FD calculations in the FD submesh, we must handle points near the injection surface S_i carefully because $\{v_i^R, \sigma_{ij}^R\}$ is discontinuous. These difficulties arise purely because the FD algorithm calculates gradients using a finite-sized stencil rather than values at a point. We must use the complete field in V_e' (adding v_i^I in the calculations) to calculate results in V_i [equation (7)]. Conversely, we must subtract v_i^I in V_i to calculate the results in V_e'' .

In each FD time step, σ_{ij}^R and the corresponding memory variables are first updated in the entire grid using systems of equations (1) and (2). When the update is complete, we correct the update at the points where the spatial FD stencil intersected the surface S_i . Here we describe how this is done for the normal stresses (illustrated in Figure 3). Inside S_i , the wavefield is updated as if the injected wavefield were propagating through the entire grid. Therefore, we must add the v_i^I components to the parts of the stencil that are outside S_i , i.e., equation (7). For a fourth-order accurate scheme, we therefore need to know v_i^I along the two closest grid points outside S_i for the lower and

right edges of the rectangular injection region shown in Figure 3, and along the closest grid point for the upper and left edges. In Figure 3, this occurs when normal stresses along the innermost thick lines (in the region with a shaded background) along each side of V_i are updated. This part of the wavefield is read from an external file where the injection wavefield is stored. Outside S_i , the wavefield is updated as if no wavefield were injected. Therefore, we must subtract the v_i^I components from the parts of the stencil that are inside S_i at points where the stencil intersects S_i [for update of normal stresses located along the outermost thick lines (in the region with a white background) along each side in V_e']. Again, this part of the injection wavefield is read from the external file.

Next, we advance the calculation by half an FD time step and update v_i^R in the entire grid by using equation (3). The wavefield injection is performed using the same procedure by adding and subtracting the stress components of the injection wavefield σ_{ij}^I at the three grid points around S_i . In total, we therefore need values of σ_{ij}^I and v_i^I stored in the external file at three grid points around S_i , staggered appropriately in time and space.

By iterating these two steps of the update, the entire FD simulation is stepped through and the wavefield stored in the external file is injected along the surface S_i .

Algorithm

A typical simulation scenario is illustrated in Figure 4. The objective of the FD-injection method is to recalculate the response of a simulation (using the outer bold box in Figure 4)

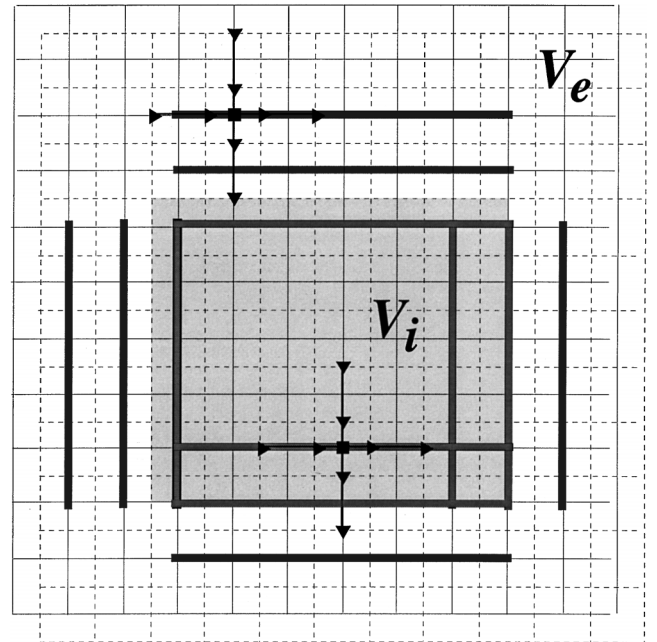


FIG. 3. Wavefield injection in the staggered FD grid illustrating the update of normal stresses. Normal stresses are located on the solid grid, whereas shear stresses are located on the dashed grid. The region with shaded background corresponds to V_i , whereas the remaining part of the grid (white background) corresponds to V_e . Two FD stencils are shown in the picture (one updating a point in V_i and one a point in V_e). A legend for the wavefield components is shown in Figure 1.

after an alteration to the dotted unit. Updating our solution only requires recalculating the part of the model inside the inner bold box in Figure 4. A flowchart for how the FD-injection algorithm may be employed is shown in Figure 5.

We begin by defining the seismic model in the full FD mesh (outer bold box in Figure 4). The compact model parameter notation \mathbf{m} denotes the stiffnesses, density, and stress and strain relaxation times throughout the model. The FD simulation then is performed with a source illustrated as a star in Figure 4. During the simulation, stresses and particle velocities are recorded (and stored in an external file) along the closed surface S_i and along the recording array S'_e (Figure 4). The wavefield also is recorded at the receivers (triangles in Figure 4). Because we are using a fourth-order accurate spatial stencil, all five components of the wavefield must be stored on three grid points around S_i , as was described above. Memory variables do not need to be stored, because no spatial derivatives of them occur.

After the full FD simulation has been completed, an alteration is introduced in the model at grid points inside the curve S_i (the dotted unit within V_i in Figure 4). In a subsequent simulation using the smaller FD submesh (inner bold box in Figure 4), we wish to calculate the response of this new altered model \mathbf{m}^c , where \mathbf{m} and \mathbf{m}^c only differ inside V_i . The wavefield recorded in the first simulation $\{v_i^I, \sigma_{ij}^I\}$ is injected into the model \mathbf{m}^c

along the surface S_i , as described in the previous section. For the case when $\mathbf{m} = \mathbf{m}^c$, the field in V_i will be exactly $\{v_i^I, \sigma_{ij}^I\}$, whereas the field in V_e will be zero, i.e., in equation (6), $v_i^R = v_i^I$ and in equation (7), $v_i^R = 0$. On S_i , the boundary conditions imposed from $\{v_i^I, \sigma_{ij}^I\}$ exactly generate the ingoing waves and cancel the outgoing waves. Equation (8) therefore reduces to $v_i = v_i^I$.

After a model alteration is made in V_i (so that the new model is \mathbf{m}^c), part of the wavefield generated in V_i will propagate through the injection surface S_i because it does not cancel with $\{v_i^I, \sigma_{ij}^I\}$. It is straightforward to show that the resulting wavefield in V_i (the region inside the dashed box in Figure 4 corresponds to the wavefield in the analogous *full* simulation using model \mathbf{m}^c (de Hoop, 1995). In V'_e , the wavefield corresponds to the difference between the wavefields from the analogous *full* simulations of models \mathbf{m} and \mathbf{m}^c , because the parts of the wavefield that correspond to $\{v_i^I, \sigma_{ij}^I\}$ are canceled along S_i .

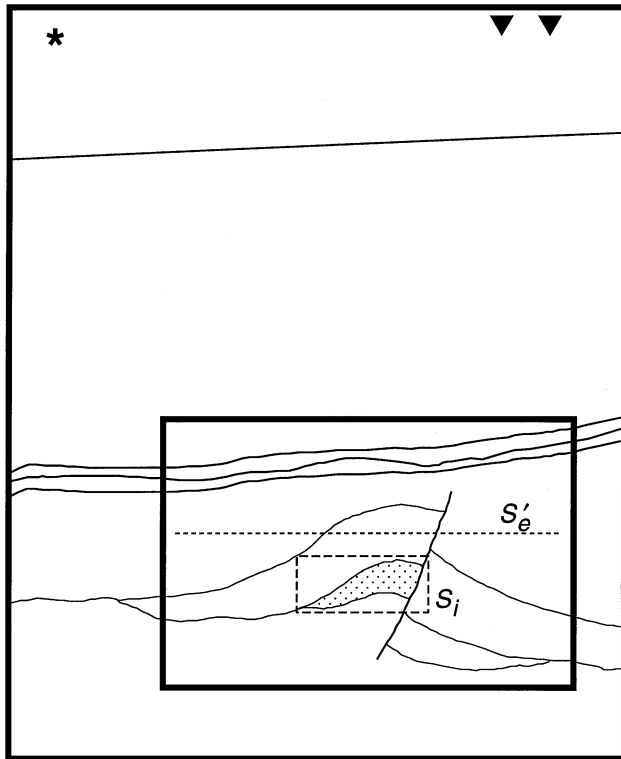


FIG. 4. Illustration of how the FD-injection technique may be employed to simulate the altered seismic response after a change to the dotted unit. The star denotes the source location. Triangles show surface receiver locations. The large outermost bold box shows the full FD grid. The small bold box shows the small FD grid to be recalculated (the FD submesh). The dashed injection surface S_i is the closed curve along which the wavefield is recorded/injected. The dashed surface S'_e is the recording array in the small simulation.

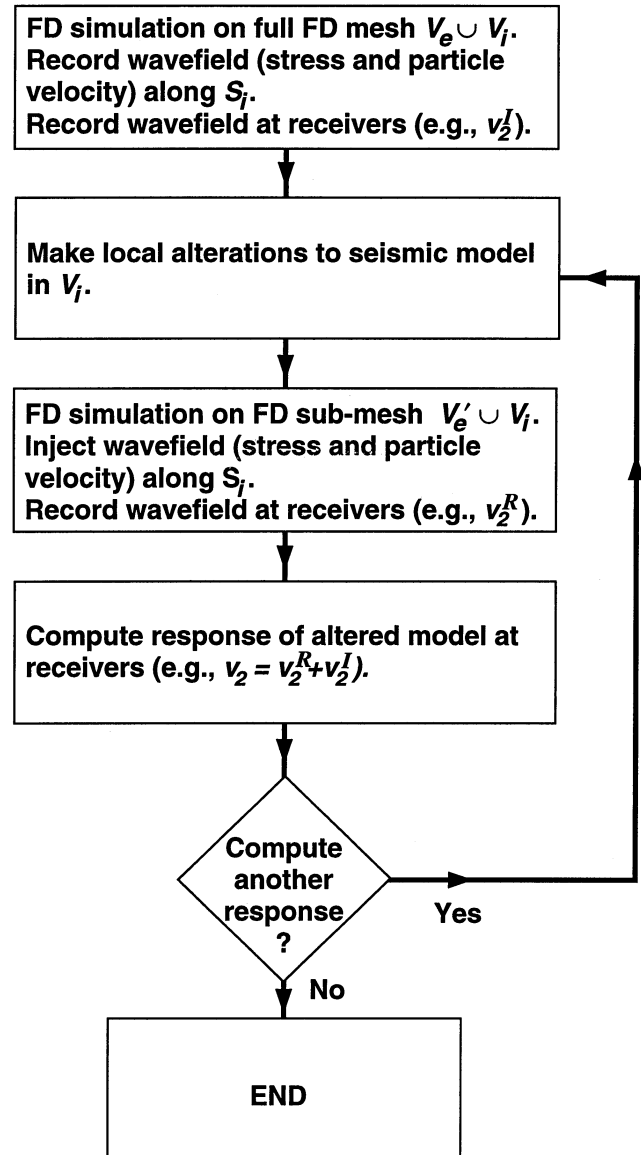


FIG. 5. Flowchart describing how the FD-injection algorithm can be employed.

Notice that the wavefield in V'_e may interact with the surrounding model and propagate back inside V_i . In this manner, we can obtain the response of the altered model \mathbf{m}^c recorded along S'_e in Figure 4 either by recording the wavefield directly in V_i or by recording it in V'_e and then adding it to $\{v_i^f, \sigma_{ij}^f\}$ recorded along S'_e in the original simulation. The resulting seismogram closely corresponds to the wavefield that would have been obtained by executing the full FD simulation using the altered seismic model \mathbf{m}^c . The only events that are not accounted for are those corresponding to an alteration in the model that leave the injection subvolume (dashed box in Figure 4), propagate outside the FD submesh ($V_i \cup V'_e$, inner bold box in Figure 4), and then reverberate back inside the FD submesh to the recording locations along S'_e —so-called long-range interactions (defined in the introduction). Note, however, that independent of how the FD submesh is chosen, the FD-injection technique is exact up to propagation times after the time of the first arrival corresponding to the traveltime from the region of change, to the absorbing boundary of the FD submesh, and back to the recording locations along S'_e .

If alterations are made to several parts of the seismic model, $\{v_i^f, \sigma_{ij}^f\}$ can be injected in the various parts simultaneously, corresponding to more than one dashed box in Figure 4.

In summary, if the volume (or area in 2-D) in which the models differ is local and small, the wavefield from the simulation using model \mathbf{m} $\{v_i^f, \sigma_{ij}^f\}$ will be injected along S_i , which can be very small. Depending on the character of the seismic model, the wavefield corresponding to \mathbf{m}^c can be calculated on a fraction of the original model, thus enabling considerable computational savings.

Propagation of wavefield to receiver locations

An optional additional step (not included in the flowchart in Figure 5) that makes the FD-injection algorithm very attractive in, for instance, FD migration of seismic data is that the corrected wavefield can be extrapolated to distant receiver locations at relatively limited computational cost. Suppose we have a relatively small number of receiver elements at the top of the model (marked by triangles in Figure 4) to which we want to extrapolate the wavefield computed through the FD-injection method. Provided that we know the wavefield along a continuous contour at depth (the dashed line marked S'_e in Figure 4) spatially and temporally sampled below the Nyquist frequency, then we can extrapolate the wavefield through the overburden using equation (8) if we know the Green's functions for the "source-receiver" pairs (the sources being along S'_e). If the number of final recording points at the top of the model (triangles in Figure 4) is smaller than the number of points needed along the continuous line S'_e , then the Green's functions can be calculated efficiently using the FD method and the reciprocity theorem. By simply placing multicomponent impulsive sources at the receiver locations and recording the response at depth, all Green's functions can be obtained (see Robertsson et al., 2000). Note that this step still maintains the high accuracy of the FD approach compared with using Green's functions calculated by asymptotic techniques (as in a hybrid technique). As a large number of full FD simulations may be necessary to calculate the "receiver" Green's functions, this methodology is computationally attractive if a large number of recalculations are needed for different models, or if the

calculations are part of a large simulation in which the Green's functions can be reused for sources and receivers.

COMPUTATIONAL EFFICIENCY

The computational efficiency (in terms of computations) C_{CPU} of the FD-injection method in 3-D may be estimated as follows. The objective is to compute the wavefield at R (distant) receivers in V''_e of K different models subject to alterations within V_i . Assume that there are N^3 grid points in the full FD mesh ($V_e \cup V_i$) and n^3 grid points in the FD submesh ($V'_e \cup V_i$), and that the simulation on the full FD mesh comprises T time steps. Using conventional FD calculations, the total cost for such a set of simulations is:

$$C_{\text{CPU}} \sim aKN^3T, \quad (9)$$

where a is a constant.

Alternatively, the FD-injection method can be used and the wavefield extrapolated to the receivers using Green's functions obtained by FD as described above. The initial FD calculation to compute the injection wavefield requires aN^3T calculations. In addition, Green's functions between the R receivers and the integration surface (of size n^2) must be computed. The reciprocity theorem may be used so that this cost amounts to $aN^3T \times \min(R, n^2)$ (assuming that the receivers record one component of the wavefield). There will also be $K - 1$ simulations on the FD submesh. Because the injection wavefield initially is zero and because we need only to complete calculations as long as the wavefield interacts with the FD submesh, the required number of time steps on the FD submesh will be t , where $t \leq T$. Therefore, $(K - 1)an^3t$ calculations are required. The wavefield then is extrapolated to the receivers using equation (8). The extrapolation amounts to $(K - 1)bn^2Rt \log t$ calculations, where b is a constant and $b \ll a$ typically. In summary, the total cost is:

$$C_{\text{CPU}} \sim aN^3T(1 + \min(R, n^2)) + (K - 1)(an^3t + bn^2Rt \log t). \quad (10)$$

For large values of K , the second term in this expression dominates, leading to computational savings on the order of a factor $N^3T/(n^3t)$.

The FD-injection method also requires intermediate storage of the wavefield on disk D . In 3-D, the injection wavefield is required on a surface. Storage of Green's functions for the extrapolation of the wavefield to the receivers [equation (8)] also is required. However, this surface is sampled considerably less densely than the FD-injection wavefield. The Green's functions therefore typically require much less space than the storage of the injection wavefield:

$$D \sim cn^2t + dn^2tR, \quad (11)$$

where c and d are constants and $d \ll c$ typically.

For a case with R sources that are coincident with the receivers, we can reuse the Green's functions, so that the cost is:

$$C_{\text{CPU}} \sim aN^3T \min(R, n^2) + R(K - 1)(an^3t + bn^2Rt \log t). \quad (12)$$

Here, the intermediate storage is

$$D \sim cn^2tR. \quad (13)$$

Note that this corresponds to the total cost for a case with K models and R shot gathers.

The analogous 2-D results can be obtained by reducing the power of all factors n and N in the above expressions by one.

EXAMPLE: TIME-LAPSE SEISMICS IN THE NORTH SEA

The method is illustrated on an example using a 2-D model developed from experiences gained over years at Schlumberger from hydrocarbon exploration in the North Sea. The model contains features that are difficult to image such as lenses, faults, and “pinch-out” structures (gradually eroded sediment sequences). The model is shown in Figure 6 (Kragh, E., 1997, personal communication) and a legend corresponding to the model is shown in Figure 7. Although the geometry is simplified, the material properties are taken from actual North Sea wells. There are two oil reservoir layers (layers 16 and 19 in Figure 7) in the model. A fault splits the two layers into four oil-bearing units. In this example, we will be concerned with the upper of the two units on the left side of the fault (Figure 6).

In time-lapse seismics, the goal is to monitor the flow of fluids in a reservoir during production. Extraction of hydrocarbons is believed to cause detectable changes in the seismic response. In particular, oil and gas are substituted by water as hydrocarbons are produced. In this example, we therefore have investigated the differences in the response from the model as shown in Figure 6 and a model where the properties of layer 16 to the left of the fault have been substituted with the properties of layer 17. In other words, a case where the oil has been substituted completely by water (i.e., full production of the unit).

The model in Figure 6 has a free surface on the top (flat sea surface) and 120-m-thick absorbing boundary conditions of a “sponge” type applied on the sides (Kosloff and Kosloff, 1986).

The star in Figure 6 illustrates the location of the source at $x_1 = 300$ m and $x_2 = 9$ m consisting of an explosive-type 40-Hz Ricker wavelet. The triangles illustrate the location of a horizontal receiver array. These may be geophones located inside a horizontally drilled well or simply serve as artificial

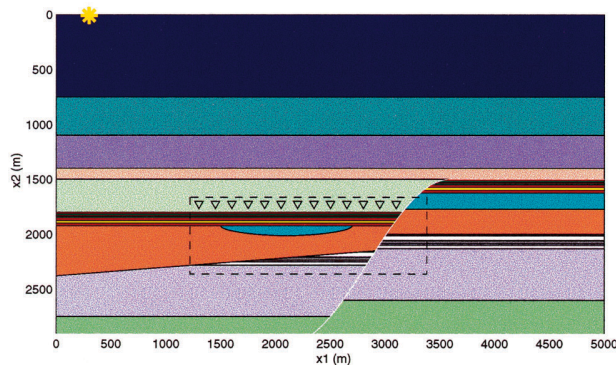


FIG. 6. Full North Sea model corresponding to the full FD mesh $V_e \cup V_i$. A legend with the different geologic units and their physical properties is shown in Figure 7. The star illustrates the location of the source. The triangles illustrate the location of the receiver array. The dashed box shows the extent of the FD submesh $V'_e \cup V_i$ (Figure 8).

reference positions to acquire knowledge of the effects of lithologic changes on the seismic response. A third possibility would be to extrapolate the field recorded along the receiver array through the (relatively simply layered) overburden. As described above, this can be done with FD precision by using FD calculated Green's functions (Robertsson et al., 2000) or by using Green's functions from another method (e.g., asymptotic ray theory or a plane-wave solution). However, in this example, we have used the simpler possibility of receivers in a horizontal well.

Figure 8 shows an enlargement of the region indicated by a dashed box in Figure 6. Inside this model we also show another small dashed box around the unit that is subject to the fluid

Log	v_p (m/s)	v_s (m/s)	ρ (kg/m ³)
1	$v_p=1500$	$v_s=0$	$\rho=1000$ (600m water)
2	$v_p=1860$	$v_s=950$	$\rho=1600$
3	$v_p=2066$	$v_s=950$	$\rho=1750$
4	$v_p=2049$	$v_s=950$	$\rho=1900$
5	$v_p=2176$	$v_s=1000$	$\rho=2089$
6	$v_p=1950$	$v_s=950$	$\rho=1800$
7	$v_p=2440$	$v_s=1108$	$\rho=2100$
8	$v_p=1950$	$v_s=950$	$\rho=1800$
9	$v_p=2440$	$v_s=1108$	$\rho=2100$
10....	$v_p=1950$	$v_s=950$	$\rho=1800$
11....	$v_p=2440$	$v_s=1172$	$\rho=2100$
12....	$v_p=1950$	$v_s=950$	$\rho=1800$
13....	$v_p=2286$	$v_s=1152$	$\rho=2144$
14....	$v_p=2751$	$v_s=1470$	$\rho=2219$
15....	$v_p=2900$	$v_s=1550$	$\rho=2400$ (12m)
16....	$v_p=2770$	$v_s=1614$	$\rho=2200$ (Oil1 45m)
17....	$v_p=2913$	$v_s=1584$	$\rho=2281$ (Water 30m)
18....	$v_p=2900$	$v_s=1550$	$\rho=2400$ (15m)
19....	$v_p=2822$	$v_s=1646$	$\rho=2180$ (Oil2 30m)
20....	$v_p=2900$	$v_s=1550$	$\rho=2400$
21....	$v_p=3000$	$v_s=1650$	$\rho=2500$

FIG. 7. Legend for North Sea model. The model is completely elastic (infinite Q). Corresponding models are shown in Figures 6 and 8.

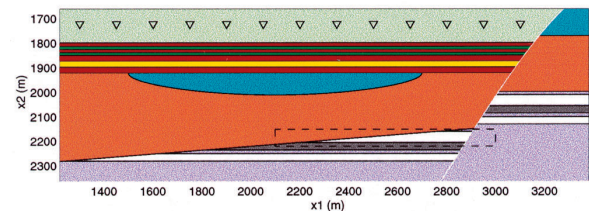


FIG. 8. Small North Sea model (location shown in Figure 6). The model corresponds to the FD submesh $V'_e \cup V_i$. A legend with the different geologic units and their physical properties is shown in Figure 7. The triangles illustrate the location of the receiver array. The dashed box around the block corresponding to layer 16 (Figure 7) shows the surface along which the source field from the full simulation is injected (the injection surface S_i).

substitution. The small model in Figure 8 is the FD submesh used in the recalculation of the seismic response after fluid substitution. The small dashed box (S_i) in Figure 8 illustrates the surface along which the wavefield is recorded in the full simulation (on the full FD mesh) and then injected into the FD submesh in the recalculations after the fluid substitution. This generates a wavefield $\{v_i^R, \sigma_{ij}^R\}$ outside the small dashed box (in V_e') that is then recorded along the receiver array (triangles).

Finite-difference simulations

In Figure 9, we show two snapshots (vertical component of particle velocity) from the FD simulation of the full model in Figure 6 (the full FD mesh) before the fluid substitution of oil by water. The first is at an early time (1.5 s) before the wavefield has interacted with the reservoir and while the wavefield still has a relatively simple structure. The second is later (3.5 s) when the wavefield has propagated throughout most of the model. Here, multiple reflections in the water column and the sedimentary layer result in a very complex elastic wavefield. Plotted on top of the snapshots, we also show the locations of the FD submesh and the injection surface S_i .

In Figure 10, we show snapshots (vertical component of particle velocity) from the FD simulation of the small model in Figure 8 (the FD submesh) before the fluid substitution of oil

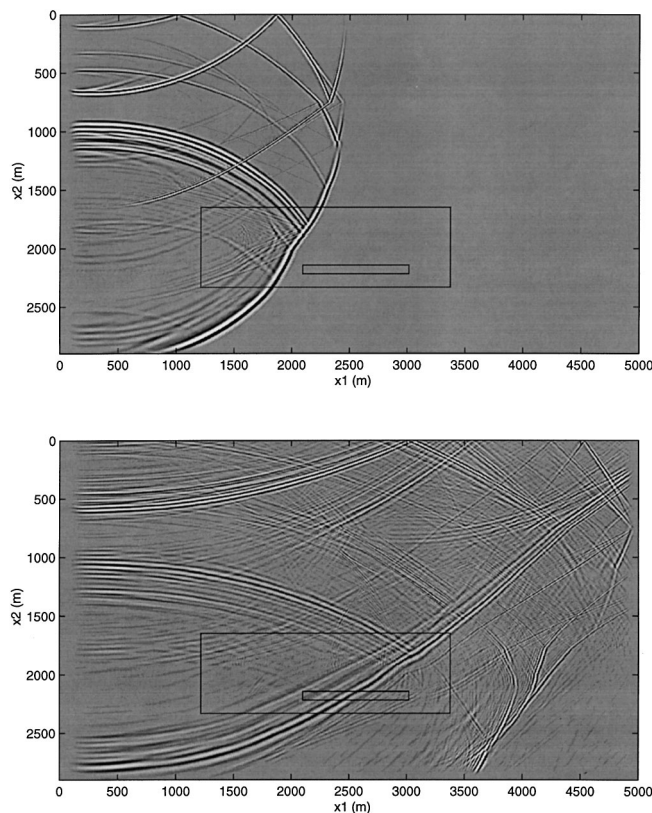


FIG. 9. Snapshots of vertical particle velocity after 1.5 s (top) and 3.5 s (bottom) using the full model in Figure 6 before oil substitution. The location of the FD submesh is shown by the larger rectangular surface (the surface S). The smaller rectangular surface inside S shows the injection surface S_i . In this initial simulation on the full FD mesh, the wavefield is recorded along S_i .

by water. Because this model is identical to the corresponding part of the full model used to generate the injected field, the wavefield inside the injection surface S_i (dashed box in Figure 8) is identical in the simulations on the full FD mesh and the FD submesh (the wavefield inside S_i is exactly the same in the bottom of Figures 9 and 10). The snapshot corresponding to the first in Figure 9 would be exactly zero, so we have postponed the first snapshot until the wavefield begins to interact with the injection subvolume (1.75 s). The second snapshot is at the same time as Figure 9 (3.5 s). The wavefield outside the injection surface S_i is as close to zero as the machine precision of the computer being used (in this case, this noise is on the order of 10^7 lower amplitude than the amplitude of the injected field).

In Figure 11, we show snapshots (vertical component of particle velocity) from the FD simulation of the small model in Figure 8 (the FD submesh) after the fluid substitution of oil by water. Because this model differs from the model used in generating the injected field, the wavefield outside the dashed box in Figure 8 now corresponds to $\{v_i^R, \sigma_{ij}^R\}$ and is nonzero. By adding this wavefield to $\{v_i^I, \sigma_{ij}^I\}$, we obtain the desired wavefield [equation (7)]. However, in time-lapse seismics, it is exactly the difference wavefield $\{v_i^R, \sigma_{ij}^R\}$ that is of interest. It is obtained by subtracting the seismic response from two more or less identical surveys to image changes in the lithology that may have occurred.

In Figure 12, we show a seismogram (vertical component of particle velocity) recorded along the line indicated by triangles in Figure 6 in the full simulation using the North Sea model before the oil substitution. The complex wavefield is caused by multiple interactions and conversions at the different interfaces, as could be seen in the snapshots from the simulation (Figure 9).

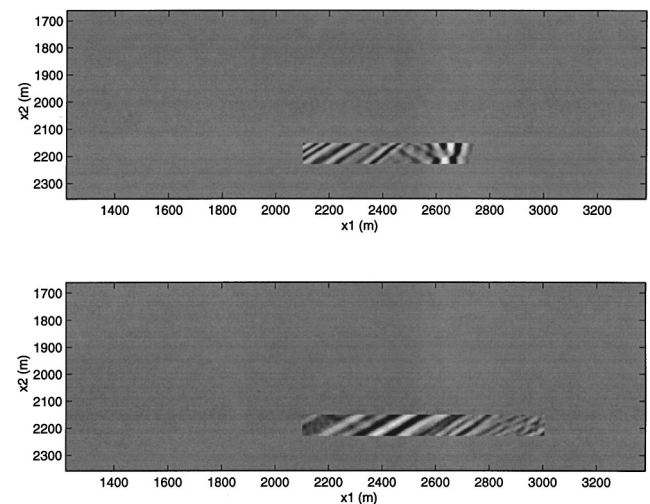


FIG. 10. Snapshots of vertical particle velocity after 1.75 s (top) and 3.5 s (bottom) using the small model in Figure 8 before oil substitution. The wavefield from the full simulation is injected along the injection surface S_i around the unit of interest. Notice how a complex wavefield resulting from interactions throughout the full FD mesh is present inside the injection surface, whereas the wavefield in the rest of the grid is as close to zero as machine precision allows. The small snapshots have been gained by a factor of two, compared with the large snapshots in Figure 9.

The traditional, and computationally expensive, way of simulating the response of the altered model is to redo the simulation completely. The corresponding section using the full model in Figure 6 after substituting the oil in layer 16 by water is shown in Figure 13. This simulation serves as a reference for validating the FD-injection method. Notice the changes of the events that correspond to reflections from the unit that is substituted by water. In Figure 14, we show the seismograms computed using the FD-injection method. Here, we have added

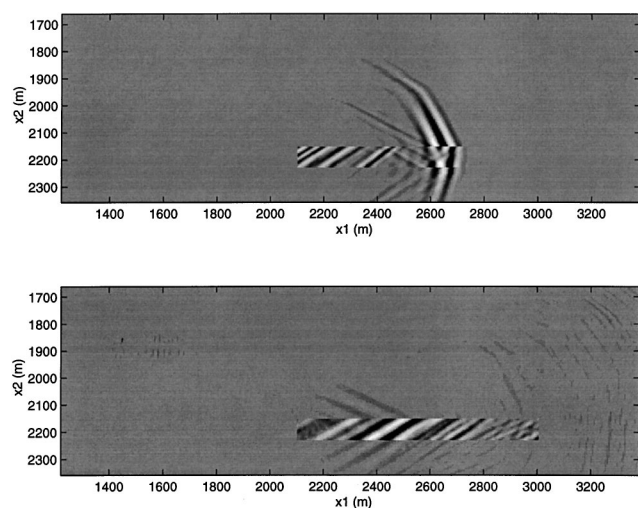


FIG. 11. Snapshots of vertical particle velocity after 1.75 s (top) and 3.5 s (bottom) using the small model in Figure 8 after oil substitution. The wavefield from the full simulation is injected along the injection surface S_i around the unit of interest. Notice how the wavefield in V_i partially leaks through S_i (as opposed to the corresponding snapshots before oil substitution in Figure 10). This part of the wavefield corresponds to the difference in the seismic response on the full FD mesh $V_e \cup V_i$ before and after oil substitution in V_i . The small snapshots have been gained by a factor of two, compared with the large snapshots in Figure 9.

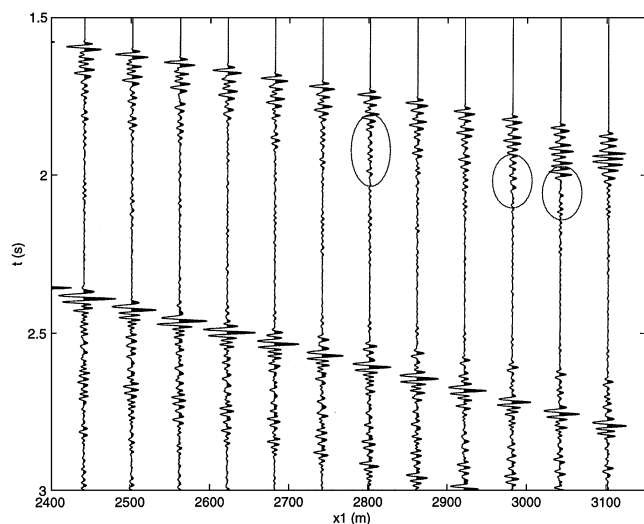


FIG. 12. Seismograms of vertical particle velocity from the simulation using the full model in Figure 6 before oil substitution. Time intervals with visible differences compared with Figures 13 and 14 have been marked along three traces.

the response from the small simulation after fluid substitution, to the response from the full simulation before fluid substitution. Figures 12, 13, and 14 are all plotted on exactly the same scale. The two seismograms in Figures 13 and 14 are visually indistinguishable, illustrating the success of the FD-injection method.

To further demonstrate the versatility of the FD-injection method, we also have plotted the difference of the recorded field from the two full simulations in Figure 15. The difference field has been amplified by a factor of 10 relative to Figures 12, 13, and 14 to increase the visibility of the differences.

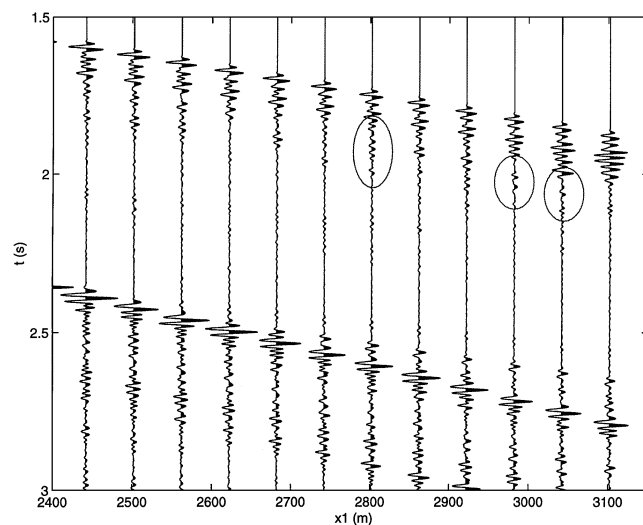


FIG. 13. Seismograms (vertical particle velocity) from the simulation using the full model in Figure 6 after oil substitution. Time intervals with visible differences compared with Figure 12 have been marked along three traces. The section was plotted using the same scaling factor as for the section in Figure 12.

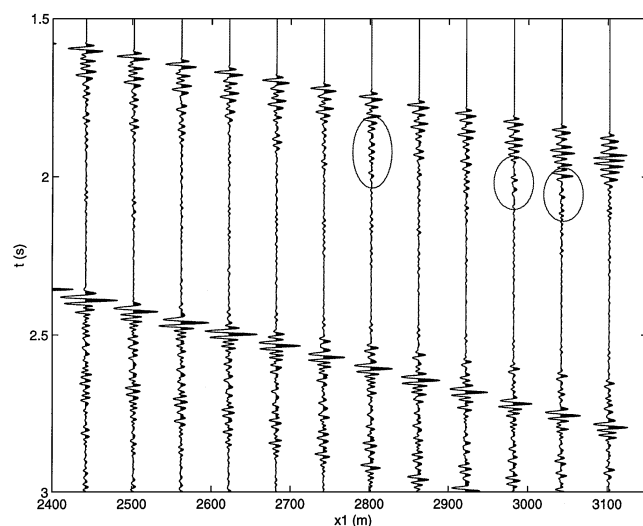


FIG. 14. Seismograms (vertical particle velocity) from the simulation for the model in Figure 6 after oil substitution. The seismograms were calculated using the FD-injection method. Time intervals with visible differences compared with Figure 12 have been marked along three traces. The section was plotted by using the same scaling factor as for the section in Figure 12.

In Figure 16, we show the response recorded directly using the FD-injection method (also amplified by a factor of 10). It is this section that is the goal in time-lapse seismic surveys. Again, the two sections are virtually identical, which is further illustrated in Figure 17, where we have plotted the difference between the seismograms shown in Figures 15 and 16 amplified by another factor of 10, i.e., a factor of 100 compared with the original seismograms (Figures 12, 13, and 14). The differences visible in the lower part of the section on this magnified scale are caused either by reflections from the absorbing boundaries or multiple interaction with features outside the smaller model, as described above. However, the first part of the wavefield is reproduced very accurately.

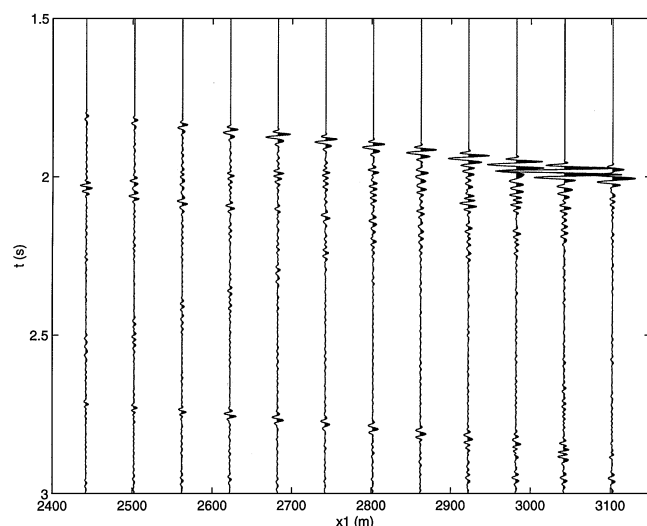


FIG. 15. Differences of the seismograms (vertical particle velocity) from the simulations for the model in Figure 6 after and before oil substitution. This section has been amplified by a factor of 10 compared with Figures 12, 13, and 14.

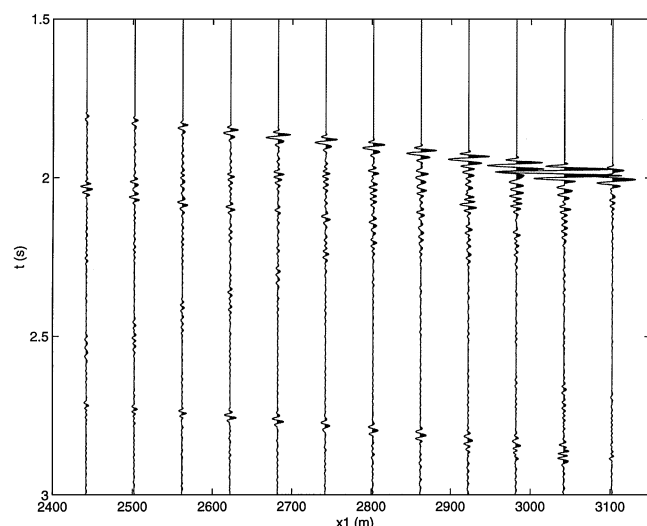


FIG. 16. Differential seismic responses (vertical particle velocity) from the model in Figure 6 after and before oil substitution. The seismograms were calculated by using the FD-injection method. This section has been amplified by a factor of 10 compared with Figures 12, 13, and 14.

We also performed a suite of simulations as the oil-water contact rises through the reservoir, using the FD-injection method. A total of 16 simulations was performed. In each simulation, the oil-water contact was raised by 3 m. In Figures 18 and 19, we show the difference during and before production recorded at two locations: $x_1 = 2622$ m and $x_1 = 2982$ m for horizontal and vertical components. The lowermost trace is 0, because this represents the simulation before production. The uppermost traces (full production) of the vertical component in Figures 18 and 19 are identical to two of the traces shown in Figure 16. In the figures, we can see how the response changes as the thickness of the oil in the reservoir decreases from 45 m to 0 m (full production). Although the seismic response changes most rapidly in the beginning (the thickness of the layer is only 45 m), some of the later events visible in the horizontal component also continue to change in character when the oil-water contact is only 15–20 m below full production (interpreted as a shear-wave arrival).

Computational cost

In the simulations using the North Sea model, the recalculation of the seismogram after fluid substitution required 9.5 times less memory than the original simulation. The savings in terms of computations were on the order of a factor of 15, because the wavefield initially is zero [cf. the 2-D equivalents of equations (9) and (10)]. For 3-D models, the savings would be even greater. If we assume that we can make similar savings along the third spatial dimension, we expect savings on the order of a factor of 30 in memory and a factor of 45 in computations [equations (9) and (10)].

In this example, we were interested in the wavefield inside the FD submesh. The computational cost for propagating the wavefield back up to the surface depends on the number of model alterations, K , and the number of receivers, R . Robertsson et al. (2000) present a time-lapse seismic case study in which the FD-injection technique was used and surface seismic and downhole measurements were considered. It

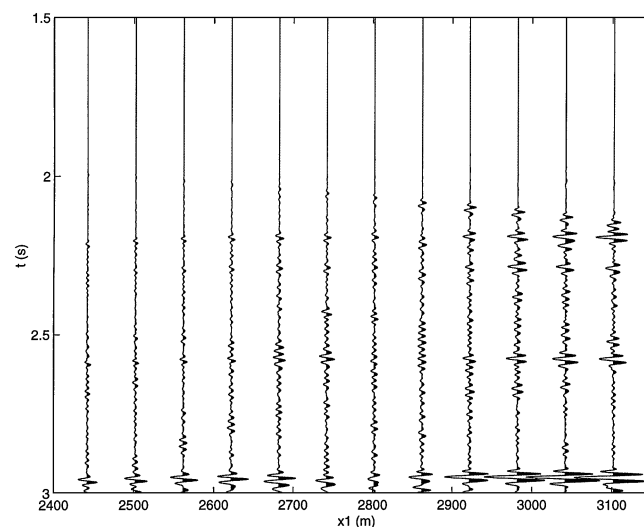


FIG. 17. Differences between the seismograms in Figures 15 and 16 (vertical particle velocity). This section has been amplified by a factor of 100 compared with Figures 12, 13, and 14.

is worth reiterating here that the extra cost of propagating the wavefield up to the surface, i.e., evaluating the representation integral in equation (8), is relatively minor provided that the receiver Green's functions are known. If the response is required for multiple sources and the receivers coincide with sources, then calculating these Green's functions introduces no extra cost.

Finally, it is worth pointing out that the surface S_i where the source field is injected often can be made very small relative to the complete original model and even the FD submesh. Thus, only a small fraction of the source field needs to be saved, often on disk, enabling long simulation times. In this example, the entire source injection field for 8000 time steps requires 389 MBytes. However, simulating the first 1.5 s of signal in Figure 14 requires 124 MBytes of disk space [equation (11)]. For comparison, optimal storage of the entire wavefield at all points and times would require about 25 GBytes in the small FD simulation and 235 GBytes in the large simulation.

DISCUSSION AND CONCLUSIONS

We have presented a new method for correcting or updating seismograms from FD simulations after alterations to the seismic model. Following initial computations on the full model (in general, one simulation for each source/receiver location), the new method, referred to as the FD-injection method, requires only recalculations of the wavefield in the vicinity of the volume (or area in 2-D) where the alteration took place. Because seismic modeling, processing, and inversion applications often require the calculation of the seismic response after incremental local alterations in small subvolumes of a seismic model, we foresee a wide variety of applications. For example:

- 1) Pre-stack FD migration/inversion of seismic data provides a highly accurate means of producing images of the Earth's interior. The migration-inversion algorithm consists of recalculating the FD response for small local

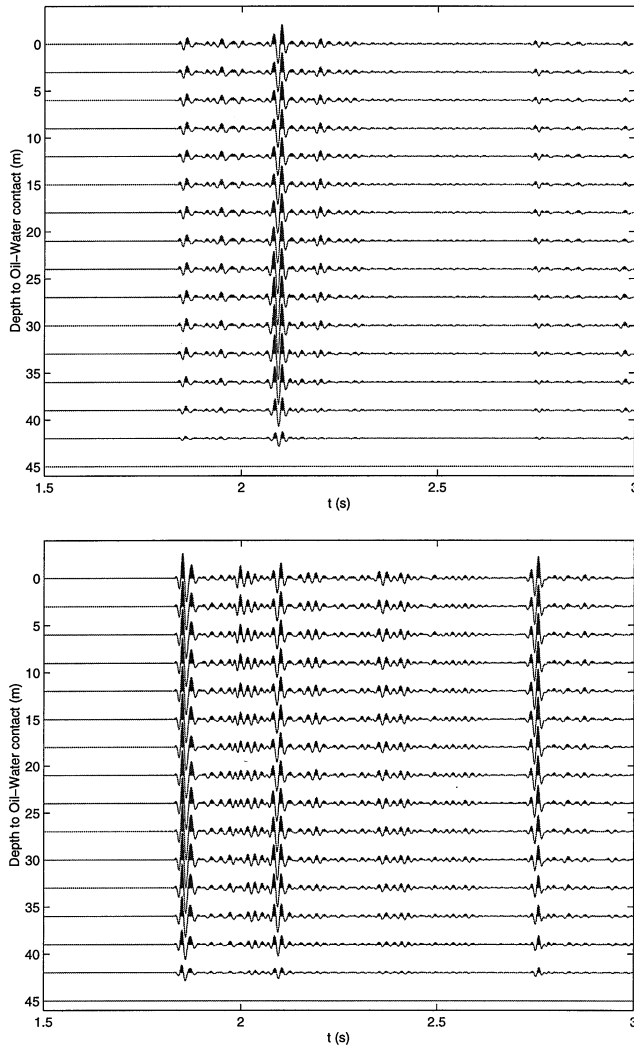


FIG. 18. Differential seismic responses recorded at $x_1 = 2622$ m in the model in Figure 6 during and before oil substitution. The traces represent the results as the oil-water contact rises through the reservoir [bottom traces are differential responses before production (zero), top traces after production]. Top: horizontal component. Bottom: vertical component.

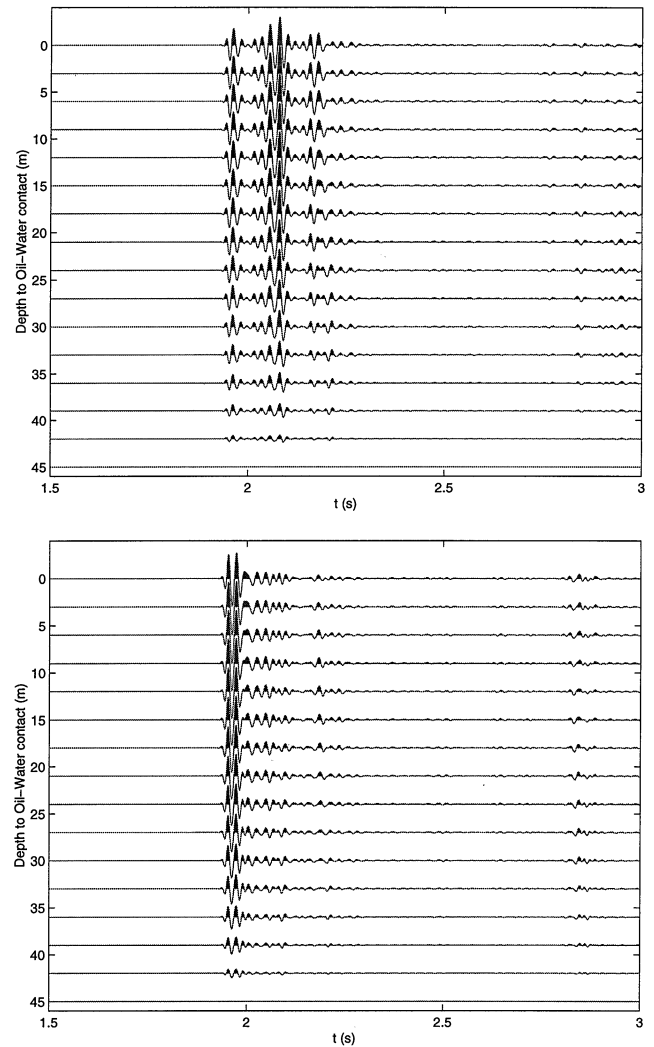


FIG. 19. Differential seismic responses recorded at $x_1 = 2982$ m in the model in Figure 6 during and before oil substitution. The traces represent the results as the oil-water contact rises through the reservoir [bottom traces are differential responses before production (zero), top traces after production]. Top: horizontal component. Bottom: vertical component.

changes to the seismic model. Unfortunately, full FD migration rarely is performed because computational limitations restrict migration algorithms to less accurate asymptotic techniques.

- 2) In FD inversion, recalculation of the FD response is the core (forward-modeling step) of the algorithms.
- 3) In time-lapse seismics (or 4-D seismics), it is of interest to investigate what effect small (local) changes to the model have on the seismic response (e.g., varying water-oil contact levels in a reservoir, as illustrated in the example in this paper).
- 4) In forward modeling, it may be of interest to recompute the response of a seismic model. Forward modeling may serve as a means of learning what effects certain features of a seismic model have on the full response. In addition, as the knowledge of the model evolves or as it becomes more refined, the simulated response may need to be updated.
- 5) In amplitude-variation-with-offset (AVO) calculations, the effects of, for instance, changes of the degree of anisotropy of a caprock may be the target of investigation.
- 6) In tools for borehole measurements, simulations of their behavior and characteristics in their operational environment provide an important aid in the design and development procedure. Typically, it is of interest to investigate the effects that small changes have on the propagation of waves in the vicinity of the tool.

The FD-injection method yields "exact" results (as far as FD methods go) after model alterations, independent of the nature of the local change (it is not based on perturbations of point scatterers). The complete interaction of the wavefield between the smaller FD submesh, where the recalculation takes place, and the full model before model alteration is accounted for totally. The only part of the wavefield missing is so-called long-range interactions (as defined in the introduction). The smaller FD submesh therefore should include the parts of the model which will reverberate scattered/reflected energy caused by the model alteration back to the recording points inside the submesh.

The method has been demonstrated by using an example from time-lapse seismics, in which the seismic response during production (a rising oil-water contact) was simulated. The computational cost of these simulations was a factor of 15 smaller than that of an analogous conventional FD simulation. In another study, Robertsson et al. (2000) obtained savings on the order of a factor of 54 when applying the FD-injection technique to a time-lapse seismics problem. Potential savings in 3-D are far greater.

ACKNOWLEDGMENTS

We thank A. K. Booer, Andrew Curtis, Adrian de Hoop, Ed Kragh, Sarah Ryan-Grigor, and Carl Spencer for many

discussions and helpful suggestions. We also thank Kun Hua Chen, Kurt Marfurt, and Jerry Schuster for useful suggestions when reviewing the paper.

REFERENCES

- Aki, K., and Richards, P. G., 1980, Quantitative Seismology—Theory and Methods: W. H. Freeman & Co.
- Alterman, Z., and Karal, F. C., 1968, Propagation of elastic waves in layered media by finite difference methods: *Bull., Seis. Soc. Am.*, **58**, 367–398.
- Blanch, J. O., Robertsson, J. O. A., and Symes, W. W., 1995, Modeling of a constant Q: Methodology and algorithm for an efficient and optimally inexpensive viscoelastic technique: *Geophysics*, **60**, 176–184.
- Chapman, C. H., and Coates, R. T., 1994, Generalized Born scattering in anisotropic media: *Wave Motion*, **19**, 309–341.
- Drake, L. A., 1972, Love and Rayleigh waves in non-horizontally layered media: *Bull., Seis. Soc. Am.*, **62**, 1241–1258.
- de Hoop, A. T., 1995, Handbook of Radiation and Scattering of Waves: Academic Press, 475–478.
- Kelly, K. R., Ward, R. W., Treitel, S., and Alford, R. M., 1976, Synthetic seismograms: A finite-difference approach: *Geophysics*, **41**, 2–27.
- Kosloff, R., and Kosloff, D., 1986, Absorbing boundaries for wave propagation problems: *J. Comp. Phys.*, **63**, 363–376.
- Kurkjian, A. L., Coates, R. T., White, J. E., and Schmidt, H., 1994, Finite-difference and frequency-wavenumber modeling of seismic monopole sources and receivers in fluid-filled boreholes: *Geophysics*, **59**, 1053–1064.
- Levander, A. R., 1989, Finite difference forward modeling in seismology, in James, D. E., Ed., *The Encyclopedia of Solid Earth Geophysics*: Van Nostrand Reinhold, 410–431.
- Marfurt, K. J., and Shin, C. S., 1989, The future of iterative modeling of geophysical exploration, in Eisner, E., Ed., *Supercomputers in seismic exploration*: Pergamon Press, Inc., **21**, 203–228.
- McLaughlin, K. L., and Day, S. M., 1994, 3D elastic finite-difference seismic-wave simulations: *Computers in Physics*, **8**, 656–663.
- Piserchia, P. F., Virieux, J., Rodrigues, D., Gaffet, S., and Talandier, J., 1998, Hybrid numerical modeling of T-waves propagation: Application to the Midplate experiment: *Geophys. J. Internat.*, **133**, 789–800.
- Pratt, R. G., 1999, Seismic waveform inversion in the frequency domain, Part I: Theory, and verification in a physical scale model: *Geophysics*, **63**, 888–901.
- Robertsson, J. O. A., Blanch, J. O., and Symes, W. W., 1994, Viscoelastic finite-difference modeling: *Geophysics*, **59**, 1444–1456.
- Robertsson, J. O. A., and Coates, R. T., 1997, Finite-difference modeling of Q for qP- and qS-waves in anisotropic media: 67th Ann. Internat. Mtg., Soc. Expl. Geophys., Expanded Abstracts, 1846–1849.
- Robertsson, J. O. A., and Holliger, K., 1997, Modeling of seismic wave propagation near the Earth's surface: *Phys. Earth Plan. Int.*, **104**, 193–211.
- Robertsson, J. O. A., Levander, A., and Holliger, K., 1996, A hybrid wave propagation simulation technique for ocean acoustic problems: *J. Geophys. Res.*, **101**, 11225–11241.
- Robertsson, J. O. A., Ryan-Grigor, S., Sayers, C., and Chapman, C. H., 2000, A finite-difference injection approach to modeling seismic fluid flow monitoring: *Geophysics*, **64**, 896–906, this issue.
- Schuster, G. T., 1985, A hybrid BIE and Born series modeling scheme: Generalized Born series: *J. Acoust. Soc. Am.*, **77**, 865–879.
- Tan, T. H., 1975, Scattering of elastic waves by elastically transparent obstacles (integral-equation method): *Appl. Sci. Res.*, **31**, 29–51.
- Wu, R. S., and Aki, K., 1988, Introduction: Seismic wave scattering in three-dimensionally heterogeneous earth, in Aki, K., and Wu, R. S., Eds., *Scattering and Attenuation of Seismic Waves*: Birkhäuser-Verlag, 1–6.
- Zahradník, J., and Moczo, P., 1996, Hybrid seismic modeling based on discrete-wave number and finite-difference methods: *Pure Appl. Geophys.*, **148**, 21–38.